Journal of Structural Biology: X 6 (2022) 100069

Contents lists available at ScienceDirect

Journal of Structural Biology: X

journal homepage: www.sciencedirect.com/journal/journal-of-structural-biology-x

SAA fibrils involved in AA amyloidosis are similar in bulk and by single particle reconstitution: A MAS solid-state NMR study

Arpita Sundaria [a,b], Falk Liberta [c], Dilan Savran [d], Riddhiman Sarkar [a,b], Natalia Rodina [a,b], Carsten Peters [e], Nadine Schwierz [d], Christian Haupt [c], Matthias Schmidt [c], Bernd Reif [a,b,*]

[a] Bayerisches NMR Zentrum (BNMRZ) at the Department of Chemistry, Technische Universität München (TUM), Lichtenbergstr. 4, 85747 Garching, Germany
[b] Helmholtz-Zentrum München (HMGU), Deutsches Forschungszentrum für Gesundheit und Umwelt, Institute of Structural Biology (STB), Ingolstädter Landstr. 1, 85764 Neuherberg, Germany
[c] Institute of Protein Biochemistry, Ulm University, Helmholtzstr. 8/1, 89081 Ulm, Germany
[d] Institute of Physics, Computational Biology, University of Augsburg, Universitätsstraße 1, 86159 Augsburg, Germany
[e] Center for Protein Assemblies, Department of Chemistry, Technische Universität München (TUM), Ernst-Otto-Fischer Str. 8, 85747 Garching, Germany

ARTICLE INFO

Keywords:
Magic Angle Spinning (MAS)
Solid-state NMR
Amyloid fibrils
Structure
Cryo electron microscopy (EM)

ABSTRACT

AA amyloidosis is one of the most prevalent forms of systemic amyloidosis and affects both humans and other vertebrates. In this study, we compare MAS solid-state NMR data with a recent cryo-EM study of fibrils involving full-length murine SAA1.1. We address the question whether the specific requirements for the reconstitution of an amyloid fibril structure by cryo-EM can potentially yield a bias towards a particular fibril polymorph. We employ fibril seeds extracted from *in to vivo* material to imprint the fibril structure onto the biochemically produced protein. Sequential assignments yield the secondary structure elements in the fibril state. Long-range DARR and PAR experiments confirm largely the topology observed in the *ex-vivo* cryo-EM study. We find that the β-sheets identified in the NMR experiments are similar to the β-sheets found in the cryo-EM study, with the exception of amino acids 33–42. These residues cannot be assigned by solid-state NMR, while they adopt a stable β-sheet in the cryo-EM structure. We suggest that the differences between MAS solid-state NMR and cryo-EM data are a consequence of a second conformer involving residues 33–42. Moreover, we were able to characterize the dynamic C-terminal tail of SAA in the fibril state. The C-terminus is flexible, remains detached from the fibrils, and does not affect the SAA fibril structure as confirmed further by molecular dynamics simulations. As the C-terminus can potentially interact with other cellular components, binding to cellular targets can affect its accessibility for protease digestion.

Introduction

Serum amyloid A (SAA) is secreted during the acute phase of inflammation (Zahedi et al., 1991; De Buck et al., 2016), and is implicated in several chronic inflammatory diseases such as AA amyloidosis (Lachmann et al., 2007; Brunger et al., 2020), atherosclerosis (Shridas and Tannock, 2019), and rheumatoid arthritis (Chambers et al., 1983). The protein is synthesized in the liver after stimulation by interleukin-6 and circulates in the plasma as apolipoprotein associated with HDL (Coetzee et al., 1986). It is believed that SAA is involved in lipid encapsulation to remove cell membrane debris from sites of injury (Gursky, 2020). During inflammation, the concentration of SAA increases 1000-fold (Uhlar and Whitehead, 1999). Under these conditions, SAA becomes unstable, aggregates, and forms fibrils that are deposited in different organs such as the kidney, liver, spleen, and heart (Sack, 2018). Renal involvement is the most frequent and serious complication of AA amyloidosis. In case infections are not treated, kidney cells loose function and become apoptotic (Lachmann et al., 2007), necessitating a renal replacement therapy including renal transplantation (Kofman et al., 2011; Sayed et al., 2015). SAA amyloid fibrils have prion-like properties and are transmissible across species (Solomon et al., 2007; Westermark and Westermark, 2009). This property turns SAA into an ideal system to study the structural mechanism of fibril seeding and prion propagation.

* Corresponding author at: Bayerisches NMR Zentrum (BNMRZ) at the Department of Chemistry, Technische Universität München (TUM), Lichtenbergstr. 4, 85747 Garching, Germany.
E-mail address: reif@tum.de (B. Reif).

https://doi.org/10.1016/j.yjsbx.2022.100069
Received 27 April 2022; Received in revised form 9 July 2022; Accepted 15 July 2022
Available online 19 July 2022

The apoprotein which is not bound to HDL adopts an α-helical structure (Lu et al., 2014). SAA is very unstable and presumably unfolded at human body temperature (Frame et al., 2017). Amyloid fibrils extracted from tissue are typically fragmented. While the full-length SAA contains 104 amino acids, protein extracted from fibrils consists mostly of the first 76 *N*-terminal amino acids (Prelli et al., 1987). However, fragments of differing lengths are found for patients with a distinctive pattern of amyloid infiltration (Westermark et al., 1989). It has been suggested that the C-terminus potentially modulates fibril structure (Rennegarbe et al., 2017) which in turn can affect protease accessibility (Stix et al., 2001; van der Hilst et al., 2008). At the same time, it is known that truncation of the C-terminus destabilizes the native fold, shifts the equilibrium towards a random coil structure, and induces faster aggregation (Tanaka et al., 2018).

Recently, the SAA fibril structure has been characterized using cryo-EM (Liberta et al., 2019a). It has been found that *in-vitro* and *ex-vivo* SAA fibril structures are distinct (Bansal et al., 2021) and that the *ex-vivo* amyloid fibril morphology can be propagated into an *in-vitro* formed

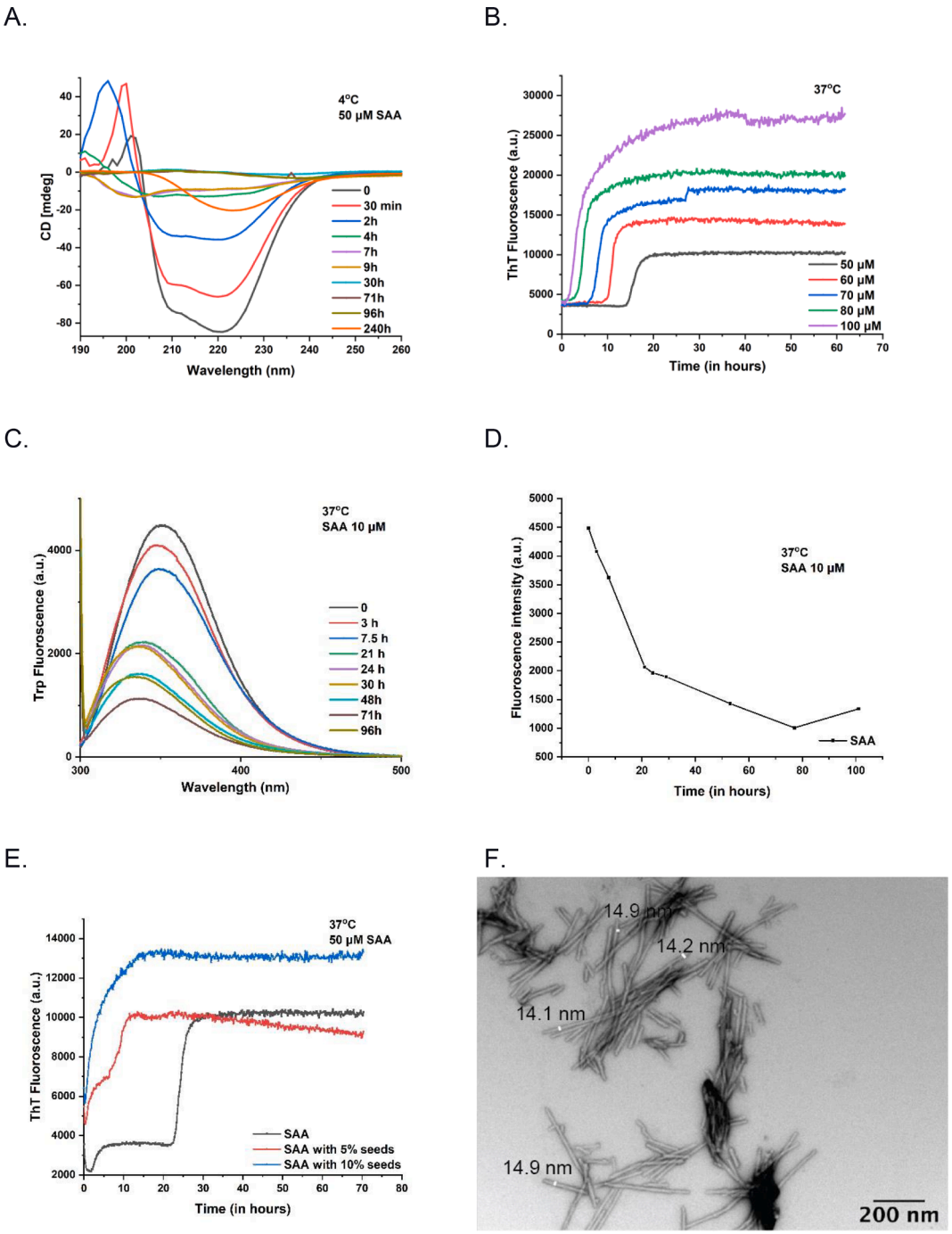

Fig. 1. Biophysical characterization of SAA aggregation. (A) CD spectra of 50 μM SAA recorded as a function of time. At 4 °C, SAA initially adopts an α-helical structure, and converts via a random coil structure into an amyloid fibril. (B) ThT aggregation assay of SAA as a function of protein concentration in the absence of seeds. (C) Tryptophan fluorescence emission spectra for a 10 μM SAA sample incubated at 37 °C as a function of time. (D) Aggregation kinetics obtained from the tryptophan fluorescence emission spectra represented in panel (C). The time scale of aggregation is similar as what is observed in the ThT experiments. (E) ThT aggregation assay for a 50 μM SAA sample in the presence and absence of seeds. (F) TEM image of SAA amyloid fibrils prepared by seeding and used for solid-state NMR experiments. The diameter of selected fibrils (marked in white) is indicated.

structure by seeding (Heerde et al., 2022). *Ex-vivo* and *in-vitro* SAA amyloid fibrils differ not only by their structure, but *ex-vivo* fibrils are also more protease stable (Schönfelder et al., 2021), suggesting that disease associated fibril polymorphs could potentially be selected inside the body by their ability to resist endogenous clearance mechanisms.

In this work, we present solid-state NMR experiments performed for SAA fibrils. The aim of our experiments is twofold: On one hand, we characterize the dynamics of the C-terminus of the protein and its interactions with the fibril core. On the other hand, we present a detailed comparison of cryo-EM and solid-state NMR data. In cryo-EM investigations, only fibrils can be analyzed which are isolated and do not stick to each other. By contrast, solid-state NMR cannot preselect a certain polymorph and yields a quantitative picture of the whole sample. Discrepancies between NMR and cryo-EM data can therefore indicate an alternative arrangement of the protofilaments or a competing configuration of the proteins in the fibril structure.

In this study, we explore the fibril formation kinetics of full-length murine SAA using CD, fluorescence spectroscopy, ThT aggregation assays, and solution-state and MAS solid-state NMR spectroscopy. We prepared *in-vitro* fibrils using *ex-vivo* tissue material as seeds. Thioflavin T experiments confirm that seeding is successful. By electron microscopy, the resulting fibrils appear homogenous and are thin with a diameter of ca. 14–15 nm. We analyzed the prepared fibrils by solid-state NMR and molecular dynamics (MD) simulations and find that the *in-vitro* prepared seeded fibrils are very similar in structure to *ex-vivo* fibrils characterized by cryo-EM.

Results

Fibril formation by murine SAA 1.1

Pure SAA is obtained after purification from recombinant expression in *E. coli*. At 4 °C (pH 8.5), SAA adopts a predominantly α-helical structure. At higher temperatures (37 °C), SAA is less stable and rapidly loses its native stable fold. We followed the aggregation kinetics of SAA by monitoring the change of the secondary structure using CD and fluorescence spectroscopy. The CD spectra show that SAA converts from an α-helical to a random-coil structure and finally adopts a β-sheet structure (Fig. 1A). This behavior is supported by Thioflavin T (ThT) data. ThT fluorescence shows a lag phase that decreases with increasing concentration (Fig. 1B). At the same time, the intensity at the plateau increases with protein concentration. In the ThT assay, we observe the same lag time as in the Trp fluorescence experiments suggesting that ThT does not act as an inhibitor of aggregation. SAA contains three tryptophans in its sequence, which we exploit to study fibril formation. We find that the emission signal intensity decreases with time and reaches a plateau after 20 h (Fig. 1C). At the beginning of the aggregation process, the high tryptophan fluorescence intensity indicates that SAA is initially unfolded and slowly converts into a structured state. At the same time, the tryptophan fluorescence is blue-shifted, suggesting that a transition to a more apolar environment occurs (Fig. 1D).

Further, we studied the effect of seeding on the ThT fluorescence. We prepared seeds by adding 5 % *ex-vivo* seeds from mice to the biochemically produced SAA to imprint the fibril structure. Seeds prepared this way were used in the ThT assay. The addition of seeds reduces the lag phase, suggesting that seeds act as templates for fibril formation (Fig. 1E). Furthermore, seeding allows to prepare a homogeneous and high-quality solid-state NMR sample. The prepared fibrils were visualized using Transmission Electron Microscopy (TEM) (Fig. 1F).

Identification of the SAA fibril core by solid-state NMR

Solid-state NMR requires a high-quality, homogenous sample for a structural investigation. We, therefore, prepared a sample using seeds from SAA infected mice. The role of seeding has been investigated in many previous studies. It was shown that seeding can increase the homogeneity of fibrils (Qiang et al., 2011; Pradhan et al., 2021). Furthermore, solid-state NMR yields structural information on the whole ensemble. In total, we prepared three samples. In the first preparation, SAA was incubated with seeds. TEM images (Fig. 1F) of this sample show homogenous, thin, short fibrils. The resulting solid-state NMR 2D $^{13}C,^{13}C$ correlation and $^{15}N,^{13}C$ correlation spectra yield well-defined cross-peaks (Fig. 2A, B). To confirm reproducibility, we prepared a second sample under the same conditions. A superposition of the obtained spectra is represented in Fig. S1. Both samples showed identical 2D $^{13}C,^{13}C$ correlation (DARR) spectra with one set of peaks for every residue. Fig. 2A, B shows 2D $^{13}C,^{13}C$ DARR and a 2D $^{15}N,^{13}C^{\alpha}$ correlation spectra. Experiments were recorded using a 750 MHz NMR spectrometer, employing a 1.9 mm MAS probe. The MAS rotation frequency was adjusted to 16.65 kHz. To yield sequential chemical shift assignments, we carried out 3D NCaCx, NCoCx, and CONCa experiments. In total, we observed 55 spin systems, out of which 44 residues could be sequentially assigned, involving residues 3–23, 24–28, 30–32, and 43–59. Residues 33–42 and 60–69 could not be sequentially assigned. This is presumably due to the fact that this region is not very well structured in the fibril state or adopts a loop conformation with increased dynamics. The NMR chemical shifts were deposited in the BNMRB under deposition code 51285. Chemical shifts are referenced using DSS as an internal standard. The assigned shifts were used as input for TALOS to yield backbone torsional angles and to confirm the credibility of the assignments. We find that the experimental chemical shifts are in agreement with the allowed Ramachandran conformational space. Furthermore, a difference of the Cα and Cβ chemical shifts between the experimental and random coil values yields the secondary structure elements as shown in Fig. 2C.

Influence of the SAA C-terminus on fibril structure

Mass spectroscopy showed that fibrils extracted from tissue contained peptides of varying lengths, while the predominant processing product consists of residues 1–76 (Westermark and Westermark, 2005; Liberta et al., 2019b). While the C-terminus of SAA in the fibril structure is heterogenous, its role for fibril formation and stability is not well understood (Maszota et al., 2015; Tanaka et al., 2018). The quantitative analysis of negative-stain TEM images obtained from *in to vitro* formed SAA(1–103) and SAA(1–76) fibrils showed that the distribution of the fibril width for the full-length protein is significantly broader in comparison to fibrils formed by the truncated protein (Rennegarbe et al., 2017). This implies that the C-terminus is potentially involved in protofilament interactions. At the same time, infrared spectroscopy suggests that the C-terminus can play a modulating role to induce variations in the structural organization of the amyloid fibrils (Rennegarbe et al., 2017).

We apply here solid-state NMR to better understand the role of the C-terminal part of SAA in the fibril structure. Solid-state NMR experiments that employ INEPT for polarization transfer (Andronesi et al., 2005) allow to identify the flexible regions in the fibrils (Fig. 2E, F). We observe many cross-peaks in the respective 2D $^{1}H,^{13}C$ correlation experiments that originate from residues in the C-terminus of SAA. In particular, four alanine peaks appear in the spectra, suggesting that the C-terminus is flexible starting from residue A60. Since the sensitivity of the experiment is low, we cannot sequentially assign the dynamic region of fibrils. However, the distinct chemical shifts of certain residues like alanine, methionine, histidine, glycine, etc. allow us to define the residue type. This way, we identified 4 alanine, 1 methionine, 1 threonine, 2 serine, 1 leucine, 3 tyrosine, and 2 histidine spin systems in the ^{1}H and ^{13}C detected $^{1}H,^{13}C$ correlation spectra. This matches exactly the number of the respective residues in the primary sequence in the C-terminal region of the protein.

In addition, we observed eight peaks in the ^{1}H detected $^{1}H,^{15}N$ correlation spectra with INEPT polarization transfer. These peaks have chemical shifts that are typical for glycine and serine residues. These

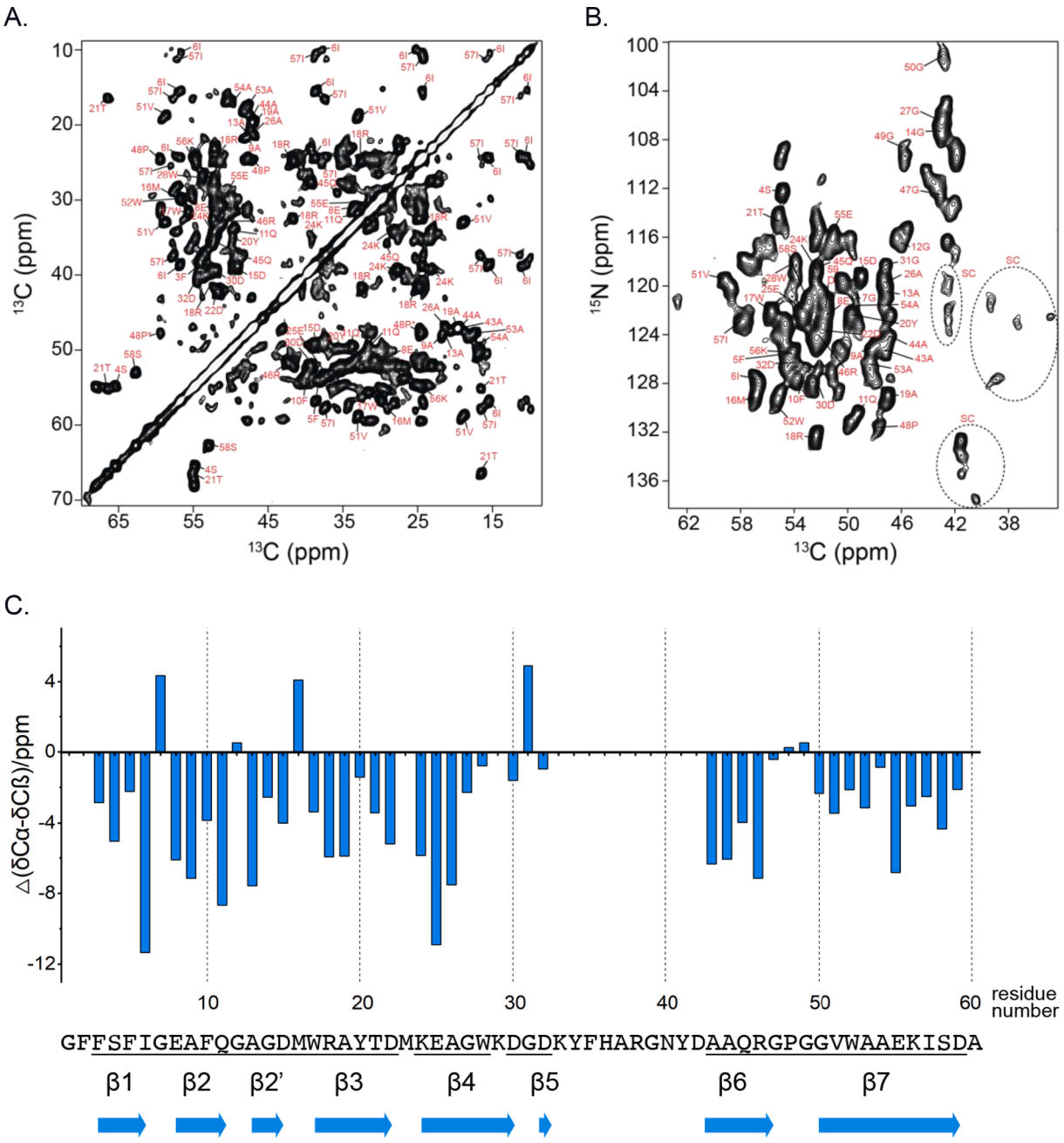

Fig. 2. Structural characterization of SAA fibrils using MAS solid-state NMR. (A) 2D-^{13}C,^{13}C DARR and (B) 2D-^{15}N,^{13}Cα correlation spectra of SAA fibrils with assignments. Chemical shifts are deposited in BMRB under the accession code 51285. SC indicates cross peaks originating from side chain resonances. (C) Secondary chemical shifts and β-sheet propensity for SAA fibrils obtained from solid-state NMR. (D) 2D strip plots showing sequential connectivities for residues M16-A19 in SAA fibrils from 3D NCACX, NCOCX, and CONCA experiments (represented in red, green and magenta, respectively). (E, F, G) Proton detected ^{1}H,^{13}C INEPT correlation spectrum, carbon detected ^{1}H,^{13}C INEPT correlation spectrum, and proton detected ^{1}H,^{15}N INEPT correlation spectrum, respectively, recorded for a SAA fibril sample in a MAS solid-state NMR rotor. Only dynamic residues are observable in these experiments. Tentative assignments are indicated with dashed circles. Average random coil chemical shifts for each amino acid type are obtained from the BMRB (https://bmrb.io/). (H) Amino acid types that are observed in the INEPT spectra are highlighted with arrows.

amino acids have the highest mobility due to the fact that they have no or very short side chains, and can therefore be observed while other amino acids cannot be detected. In total, we identify-five glycines, two serines and one threonine which is consistent with the number of these amino acids in the C-terminal region of SAA. Apparently, all residues of the SAA C-terminus beyond residues A60 can be observed in the INEPT spectra. The C-terminus thus does not seem to be important for the SAA fibril structure. We conclude that the C-terminus exclusively affects the stability of the monomeric protein. Proteolytic digestion of the monomer enhances the rate of fibril formation (Rennegarbe et al., 2017), while the C-terminus in the fibril state seems to have no protecting role against degradation. It remains to be seen how other factors such as proteoglycans affect the structure and dynamics of the SAA C-terminal region *in vivo*.

Comparative analysis of solid-state NMR and cryo-EM data

According to the solid-state NMR chemical shifts, the fibril structure

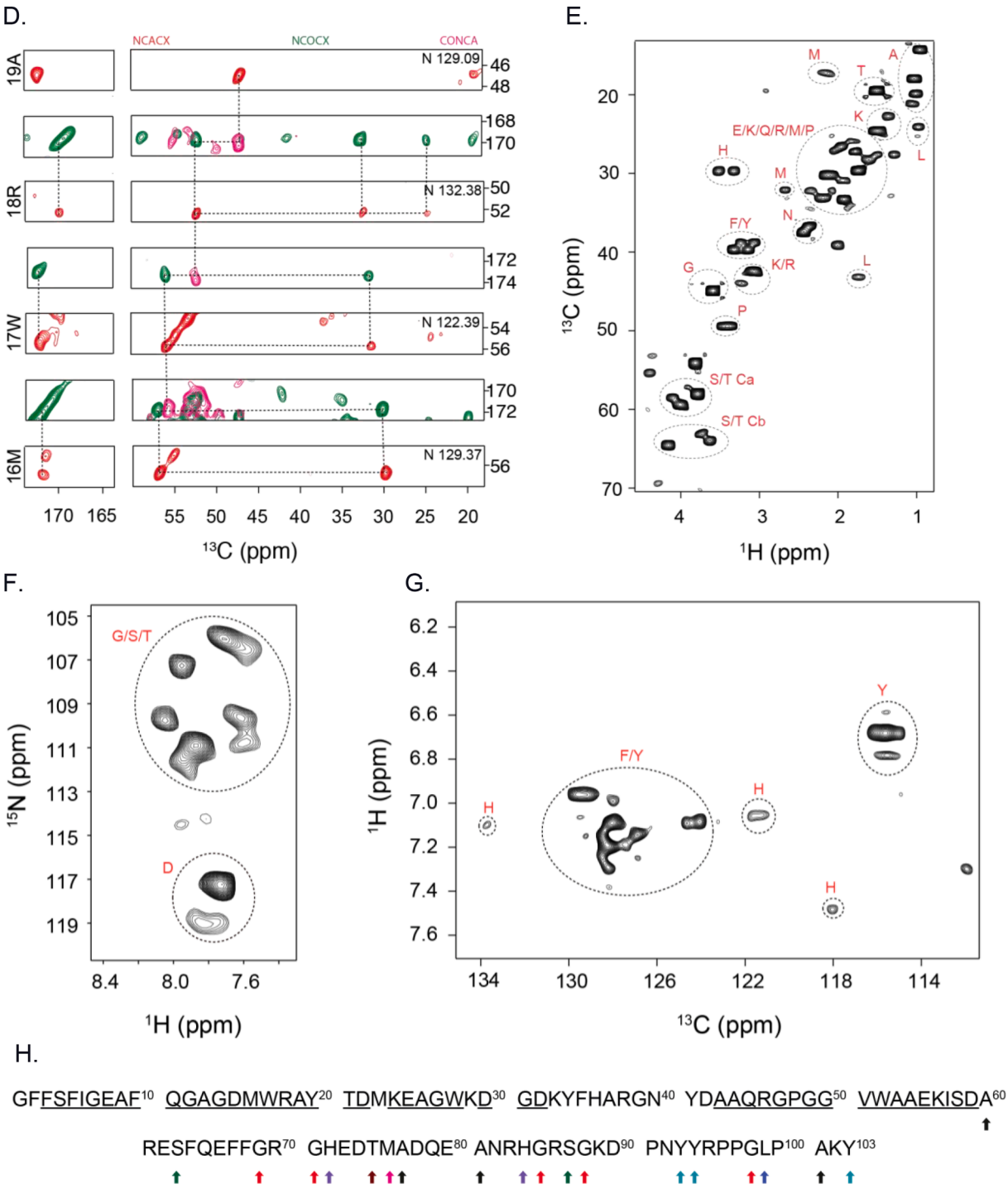

Fig. 2. (*continued*).

is composed of six β-sheets (Fig. 3A) which agrees with the β-sheets inferred from the *ex-vivo* cryo-EM structure (PDB ID: 6dso/ 6zch), with the exception of the lengths of a few β-sheets. In the solid-state NMR sample, the 3rd and 6th β-sheet is longer and includes the residues W17-22D and A43-R46. In addition, there is an additional small β-sheet (labeled as β2′) in the solid-state NMR consisting of the residues A13-D15. However, residues 33–42 and 60–69 cannot be assigned, suggesting that the 5th and 9th β-sheet from the cryo-EM structure are distinct in the NMR sample preparation.

Next, we performed experiments to probe long-range connectivities to yield structural information on the three-dimensional topology of the fibrils. In particular, we performed long mixing-time DARR (Takegoshi et al., 2003) as well as PAR (De Paëpe et al., 2008; Donovan et al., 2017) experiments. We could identify a few long-range contacts that could be unambiguously assigned. Fig. 3B shows cross-peaks involving connectivities for residues Y20-W28, I6-V51, F10-W17, E8-R46, and R18-D30. These long-range interactions are in agreement with the cryo-EM fibril structure, suggesting that the seeded *in-vitro* prepared fibrils adopt a similar structure as the *ex-vivo* fibrils.

Next, we asked the question why no sequential connectivities are obtained for those residues which are well defined in the cryo-EM model. In general, no or broad NMR resonances are observed in regions of increased flexibility or if two or more alternative configurations exist. To test whether the regions that are not visible by NMR display

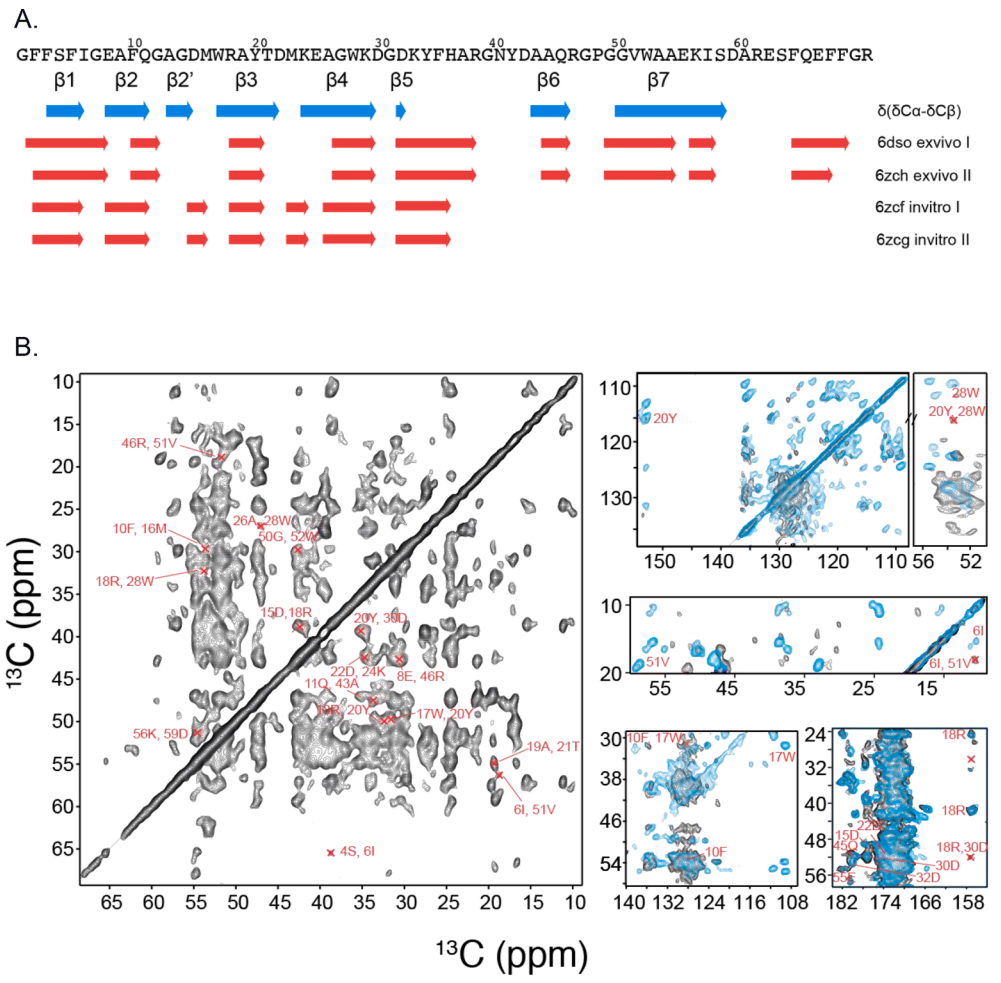

Fig. 3. Comparison of the SAA fibril topology from solid-state NMR and cryo-EM. (A) Secondary structure elements of SAA fibrils from solid-state NMR and cryo-EM (Liberta et al., 2019a; Bansal et al., 2021). (B) Long-range distance contacts in SAA fibrils were observed in solid-state NMR experiments. The small panels highlight the cross-peaks involving Y20-W28, I6-V51, F10-W17, and R18-D30, respectively. (C) Cryo-EM ex-vivo fibril structure (PDB ID: 6dso). Residues that could be sequentially assigned by MAS solid-state NMR are highlighted in grey. Long-range distance restraints from NMR experiments are indicated by dashed lines.

increased structural fluctuations or even adopt alternative configuration, we performed all-atom molecular dynamics simulations. The simulations were done for four different fibril structures: The cryo-EM *ex-vivo* fibril structure with morphology I and II (PDB ID: 6dso and PDB ID: 6zch) and two models with an alternative protofilament interface (Fig. 4A). In the first model, the interface is formed between amino acids E25 and K29. In the second model, the interface is formed between amino acids E25-K24-D22-G1-E55-K56-D59-R61. The second model is motivated by our TEDOR experiments, in which we observe two arginine and three lysine side chains to be highly ordered (Fig. S2). The observation of a larger number (>3) of immobilized charged side chains can be explained by assuming a differential packing arrangement of two protofilaments such that they are no longer solvent exposed. All four fibrils remain stable after 100 ns of simulation. Despite the different morphologies, the structure of the central peptide chains is almost identical to the cryo-EM structure 6dso. For a chain from the fibril core, the RMSD values are 1.9 ± 0.1 Å (6dso), 2.1 ± 0.1 Å (6zch), 1.95 ± 0.1 Å (model 1) and 2.4 ± 0.2 Å (model 2). In all four cases, the largest deviations are caused by the residues in the C-terminal region (Fig. 4B). The root mean square fluctuations (RMSF) provide further insights into the conformational dynamics of the different fibril morphologies (Fig. 4C). Overall, our results show that the fluctuations are similar for all four fibrils and that alternative interfaces between the protofilaments do not cause a significant change in the dynamics except for K24, which displays reduced flexibility due to its involvement in a protofilament interface in model 2. Residues 3–22 and 42–55 are in the core of the amyloid fibril structure and are flanked by β-strands on both sides leading to lower fluctuations in that region. By contrast, residues K29, H36 and R38 are solvent exposed and show the largest fluctuations. Based on the results, we conclude that the absence of NMR resonances for residues 33–42 is unlikely to be caused by a higher conformational dynamics in that region. It is rather likely, that these residues can adopt an alternative configuration. However, the different configurations might be separated by a high energy barrier and are not accessible on the timescale of the MD simulations.

Dynamics of aromatic rings

SAA contains many aromatic residues in the *N*-terminal part of the protein, and interactions among these residues presumably play an important crucial role in the aggregation process. We observe distinct peaks in the aromatic region of the 2D $^{13}C,^{13}C$ correlation experiment, suggesting that the aromatic side chains are well ordered in the core of the fibril (Fig. 5A,B). In particular, we find that the side-chain aromatic ring of Y20 becomes immobilized in the core of the SAA fibril structure. Distinct resonances for the ε1/ε2 carbon chemical shifts are observable.

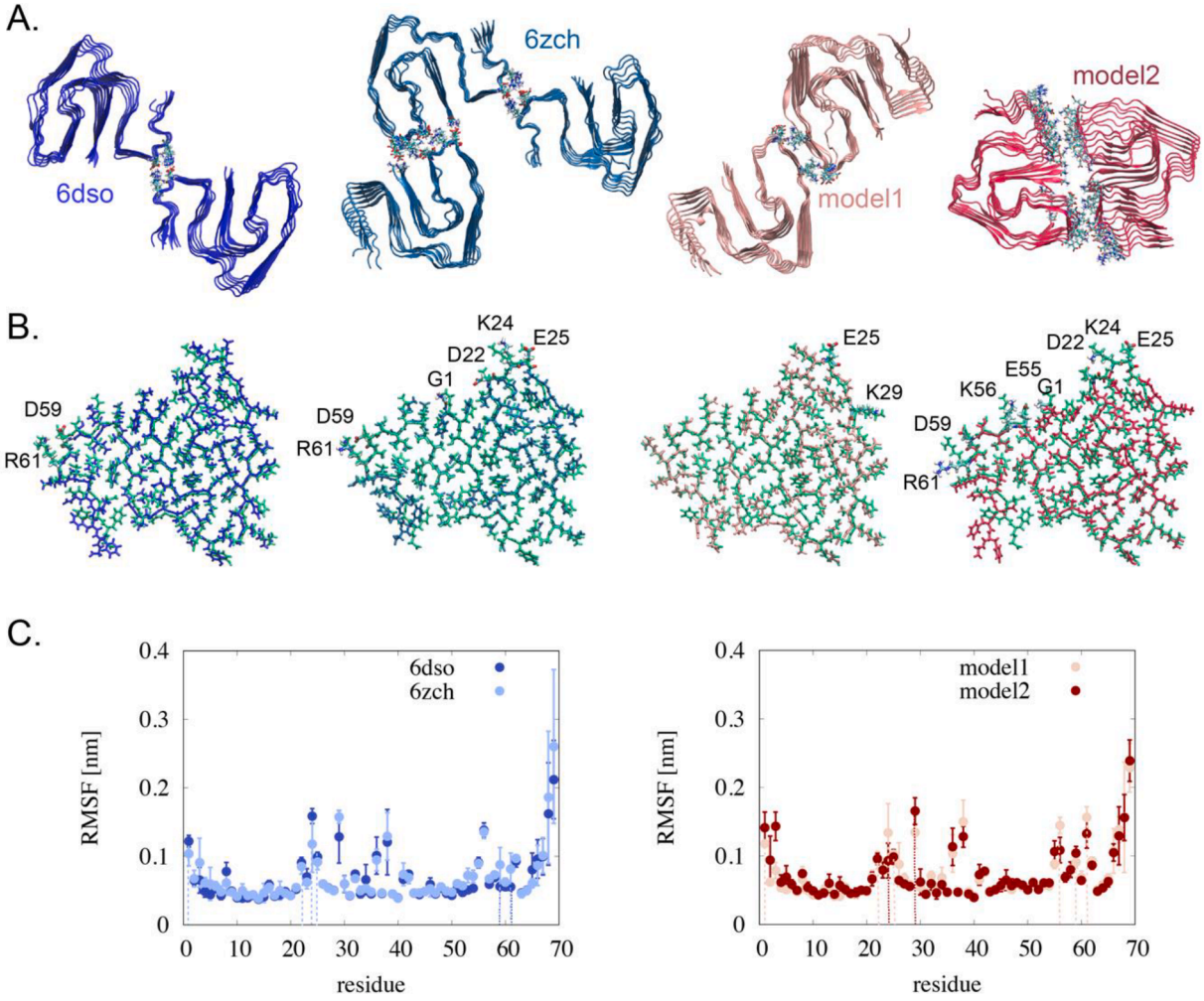

Fig. 4. Structure and conformational dynamics from MD simulations. (A) Simulation snapshots of the four fibril structures after 100 ns: 6dso, 6zch, model 1 and model 2. Residues at the protofilament interface are shown in licorice representation. Interfaces involve the following amino acids; 6dso: D59, R61; 6zch: G1, D22, K24, E25; model 1: E25, K29; model 2: G1, D22, K24, E25, E55, K56, D59, R61. (B) Superposition of one central chain of simulated structures after 100 ns and the experimental cryo-EM structure 6dso (shown in green). (C) RMSF averaged over each residue for the experimental cryo-EM structures 6dso and 6zch (left) and the two models with alternative interface (right). Error bars correspond to standard deviations. Dashed vertical lines indicate the residues at the interface.

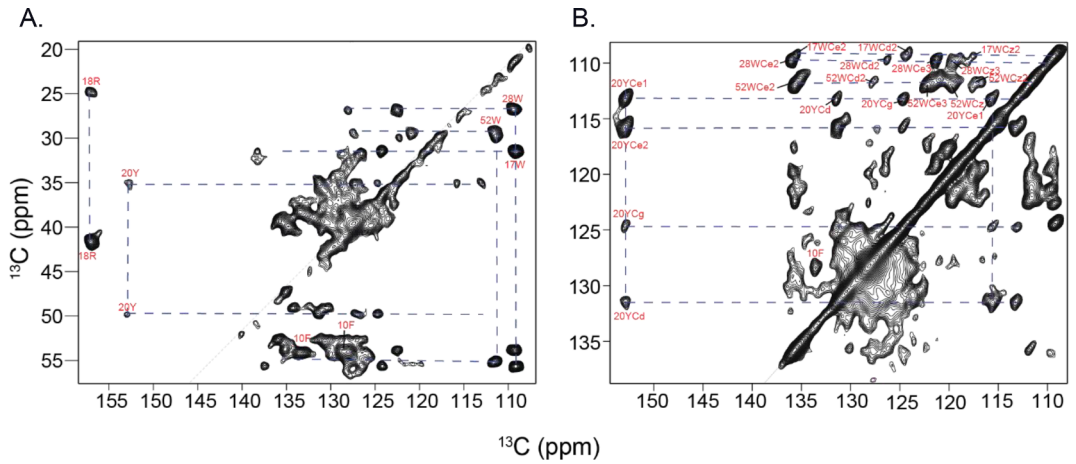

Fig. 5. Aromatic region of the 2D ^{13}C,^{13}C (DARR) correlation spectrum obtained for SAA fibrils. The spectral region containing (A) aliphatic–aromatic and (B) aromatic-aromatic cross-peaks. Distinct resonances for Y20-Cε1 and Cε2 chemical shifts suggest that the aromatic ring of Y20 is rigid. At the same time, the aromatic spin systems of W17, W28, and W52 are well resolved, while H36 and H72/H84 cannot be observed.

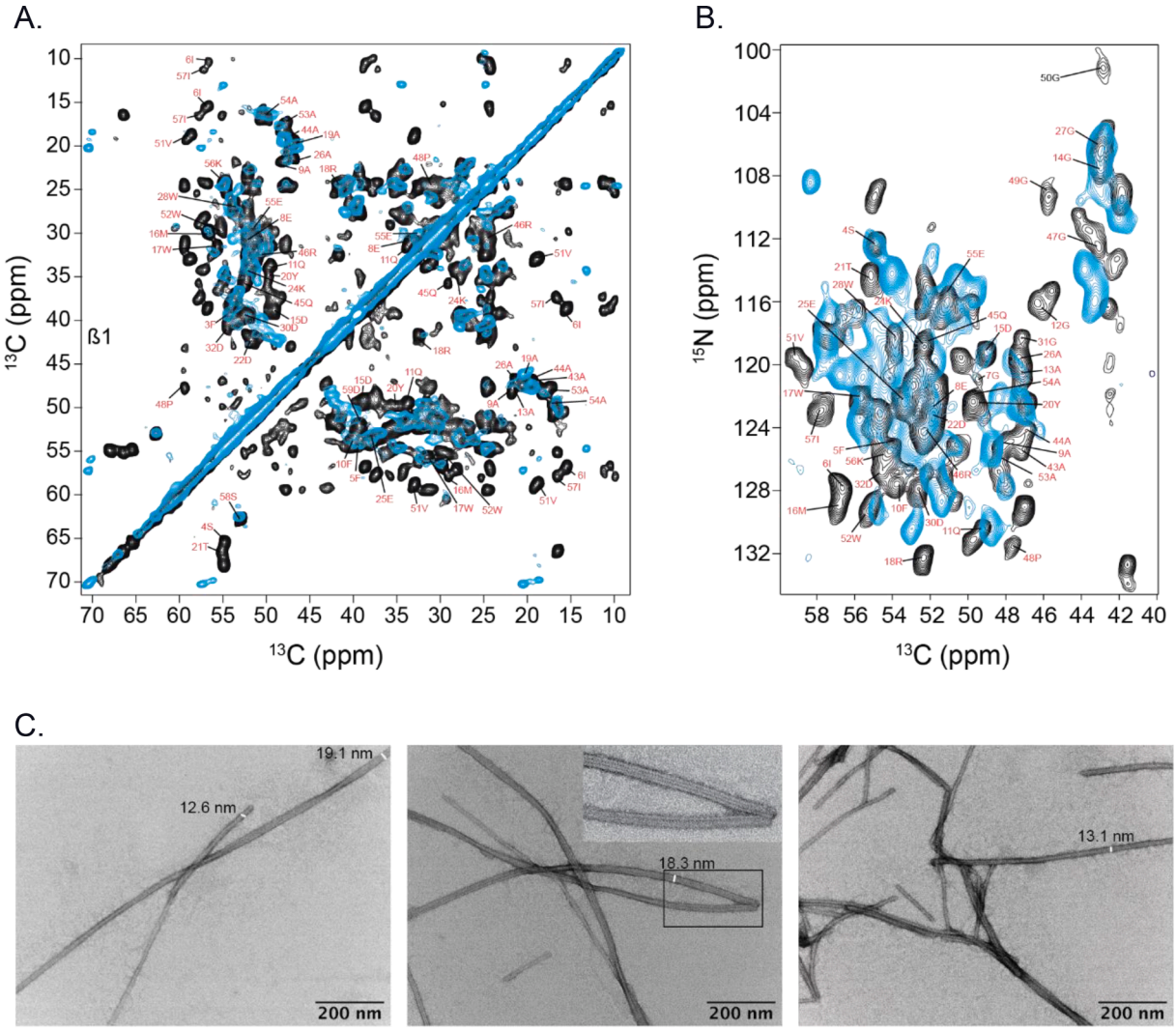

Fig. 6. Superposition of solid-state NMR spectra obtained for seeded (black) and non-seeded SAA fibril (blue) preparations. (A) 2D ^{13}C,^{13}C DARR and (B) 2D ^{15}N, ^{13}Cα correlation spectra. Tentatively assigned cross-peaks of the non-seeded sample are labeled in red. (C) TEM images of non-seeded fibrils. We observe two classes of fibrils. Fibrils consisting of three protofilaments yield a diameter of ca. 18–19 nm. Thinner fibrils that contain two protofilaments have a diameter of ca. 12–13 nm.

By contrast, other tyrosine spin systems of e.g. Y34 or Y41 are not observable. This finding is in agreement with the structure observed by cryo-EM. Y20 points into the core of the fibril, while the side chains of Y34 and Y41 are solvent-accessible.

Influence of seeding on the fibril structure

To study the effect of seeding on the structure of SAA fibrils, we prepared *in-vitro* fibrils from purified mSAA. Except for the addition of seeds, conditions were kept the same as described above. TEM images of non-seeded SAA fibrils show a distinct morphology in which 2–3 protofilaments adopt a diameter on the order of 25 nm, and seem to be bundled together to constitute a mature fibril (Fig. 6C). The fibrils are twisted and adopt a ribbon form, which is very different from the thin seeded fibrils obtained for the seeded preparation (Fig. 1B). In solid-state NMR spectra, resonances of the non-seeded fibrils are broad relative to the line width of the seeded fibrils, which suggests that this sample is more heterogeneous and polymorphic in comparison to the seeded sample. Superposition of the 2D $^{13}C,^{13}C$ DARR correlation spectra shows that the non-seeded preparation is in fact rather heterogeneous (Fig. 6A). S58 which produces only one peak in the seeded sample seems to be split into four peaks in the non-seeded fibril preparation. The matching of the chemical shifts for one of the cross-peaks for S58 must be by coincidence since no superimposing cross peak for the neighboring residues is observed. Similarly, the only threonine in the *N*-terminal part of the protein, T21, yields three peaks instead of one. The shifts of T21 do not match with the resonance frequencies obtained in the seeded sample. Overall, the non-seeded fibrils yield a smaller number of cross-peaks in comparison to the seeded fibril sample, suggesting that the core of non-seeded fibrils is smaller than the core of the seeded fibrils. This is in agreement with the cryo-EM data, in which the core of the non-seeded preparation only contains residues 1–37, and in contrast to the *ex-vivo* preparation, in which residues 1–69 are found to be well structured. Differences in the chemical shifts for seeded and non-seeded SAA fibril preparations are in agreement with the cryo-EM data for these two samples. Even though both models adopt in-register parallel β-sheet structures, their topologies differ significantly. While the *N*-terminal residue G1 is involved in a salt bridge with D22 in the non-seeded preparation (6zcf, 6zcg), G1 is sandwiched between strands β-1 and β-3 in the *ex-vivo* SAA fibril model (6dso, 6zch).

Conclusion

In this study, we compared MAS solid-state NMR spectra with a previously published *ex-vivo* SAA fibril cryo-EM structure. We successfully prepared multiple SAA fibril samples using seeds extracted from infected mice. The extracted fibrils catalyze amyloid formation and yield a diminished lag phase in ThT assays suggesting that the *ex-vivo* fibril structure can be imprinted onto the biochemically produced protein. The seeded fibril samples yield high-quality solid-state NMR spectra, which were sequentially assigned and utilized to map secondary structure elements. The β-sheets identified in the NMR experiments are similar to the β-sheets found in the cryo-EM study, with the exception of amino acids 33–42 and 60–69. These residues cannot be assigned by solid-state NMR, while they adopt a stable β-sheet in the cryo-EM structure. Otherwise, we find that the fold that is deduced from long-range interactions obtained from DARR and PAR experiments is consistent with the cryo-EM structure. We hypothesize that the differences between MAS solid-state NMR and cryo-EM data are a consequence of a second competing configuration of amino acids 33–42 that was not resolved in the cryo-EM experiments.

To explain the discrepancies between the solid-state NMR data and the cryo-EM structures, we propose two alternative protofilament packing arrangements and use MD simulations to investigate their stability and conformational dynamics. The alternative arrangements are motivated by the fact that the fibrils in amyloid plaques are densely packed and alternative protofilament interfaces between charged residues might be favored. Since the reconstruction requires a certain homogeneity in the appearance of fibrils, such alternative arrangements can remain unresolved in the cryo-EM experiments. The MD simulations that were run for 100 ns for each model show that the alternative arrangements remain stable on the timescale of the simulations. Despite the alternative interfaces, the structure of the central peptide chains remains almost identical to the cryo-EM structure 6dso. In addition, the root mean square fluctuations reveal that the conformational dynamics is similar for the different protofilament arrangements. However, the large configurational changes that induce the line broadening observed in the NMR experiments could not be sampled since the timescale of such large changes would be on the micro-to-millisecond timescale and remain out of reach for conventional MD simulations.

We find furthermore that non-seeded fibrils are less compact than seeded fibrils. Seeding appears to provide a larger interaction surface to attach monomers more effectively which finally yields a more compact structure.

Using INEPT type experiments, we were able to characterize the dynamic C-terminal tail of SAA in the fibril state. The C-terminus is flexible, remains detached from the fibrils, and does not affect the SAA fibril structure. As the C-terminus can potentially interact with other cellular components, binding to cellular targets can affect its accessibility for protease digestion.

The current study represents a step toward a better understanding of the mechanism of fibril formation by SAA. It remains to be seen which cellular factors potentially interact with the C-terminus of SAA, and how this interaction potentially affects the processing with enzymes.

Materials and methods

Expression and purification of mSAA 1.1

mSAA 1.1 was recombinantly expressed in *E.coli* using ^{13}C and ^{15}N labeled minimal media. The coding region for mSAA1.1 was cloned into a pMAL-c2 vector with a his-tagged (His_{11}) maltose-binding protein (MBP) at its *N*-terminus separated by a tobacco etch virus (TEV) protease cleavage site. Protein expression was induced using 1 mM IPTG at an OD from 0.6 to 0.7, and allowed to grow for 6 h at 37 °C. Purification was performed as described earlier (Bansal et al., 2021). In brief, the harvested cells were lysed using a French press in 20 mM Tris buffer, pH 7.5. After centrifugation, the cell lysate was purified using an MBP binding column employing a linear gradient of 0–100 % of a 10 mM maltose solution in Tris buffer. Subsequently, the eluent was purged through a metal chelate column. The protein was eluted using a 0–250 mM gradient of imidazole in Tris. Next, the protein was incubated at 34 °C overnight using TEV protease. The pure protein was separated from its tag using metal chelate chromatography. Reverse-phase chromatography using a source-15 column (GE Healthcare) running a 0–86 % linear gradient of acetonitrile was employed to yield the pure protein. The purified protein was lyophilized for further use.

CD and fluorescence spectroscopy, Thioflavin T (ThT) assay

CD experiments were carried out at room temperature employing a JASCO spectropolarimeter. Quartz cells with a path length of 0.1 cm were used. Spectra were recorded between 260 nm and 190 nm at 0.1 nm intervals, with a response time of 1 s. For the analysis of the data, the background buffer was subtracted and the data were expressed as mean residue ellipticity $\theta_{MRW} = (\text{deg cm}^2\text{dmol}^{-1}) \times 10^{-6}$. Samples were taken at different time points setting the temperature to 4 °C. Fluorescence experiments were carried out in Jasco Fluorescence Spectrometer. Prior to the experiment, the incubated protein was diluted to 10 μM. Intrinsic tryptophan fluorescence emission spectra were measured using an excitation wavelength of 295 nm. The experiments were carried out at a temperature of 37 °C. Thioflavin T (ThT) assays were performed to

investigate the kinetics of amyloid fibril growth. SAA was incubated at 37 °C using a 96-well plate (Corning, Thermo Fisher) at concentrations in the range of 50–100 μM. Orbital shaking was applied to 96-well plates after the addition of 10 μM ThT. Fluorescence was analyzed using a microplate reader (Tecan). After excitation at 440 nm, the ThT emission spectra were monitored at 480 nm as a function of time. In addition, the kinetics of seeded fibril growth was studied after adding 5 % w/w SAA fibril seeds under otherwise identical conditions.

Preparation of the solid-state NMR sample

The non-seeded fibril sample was prepared by incubating SAA at 37 °C at a concentration of 50 μM in 20 mM Tris at pH 8.5 in a shaker at 120 rpm for 10–14 days. 10 mg of protein is employed to prepare a solid-state NMR sample. The obtained fibrils are packed into a 1.9 mm ZrO_2 rotor (Bruker), using a rotor packing device from Giotto Biotech. The packing tool was placed into a Beckman Coulter ultracentrifuge using a SW32Ti swinging bucket rotor. The centrifuge was operated at 28.000 rpm, yielding direct sedimentation of the fibrils into the MAS solid-state NMR rotor. The seeded sample was prepared similarly, with the exception that 5 % w/w *ex-vivo* seeds were added to the 50 μM SAA protein solution to catalyze fibril growth. 0.02 % sodium azide was added to all the samples to avoid bacterial growth.

Transmission Electron Microscopy (TEM)

Fibrils were characterized by Transmission Electron Microscopy (TEM), using carbon-coated Formvar supported copper grids (Ted Pella, Inc.). Grids were glow-discharged for 30 s before applying the samples. 5 μl of the sample were incubated on the grid for 1.5 min, then blotted off with filter paper. Subsequently, the grid was washed two times with a few drops of distilled water. The remaining liquid was wicked off. Afterwards, 5 μl of 2 % uranyl acetate was applied to the grid. The staining solution was removed with filter paper after a 30 s incubation time. The grid was allowed to dry for 10 to 15 min before imaging. Micrographs were taken with a Ruby camera installed in a JEOL 1400 plus microscope (JEOL) operated at 120 kV at a nominal magnification of 60 k, which resulted in a pixel size of 0.275 nm/px. The scale bar was added using the software IMAGE J 2.

Solid-state NMR experiments

The solid-state fibril samples were measured at a magnetic field strength of 17.6 T (corresponds to a ^{1}H Larmor frequency of 750 MHz). The measurements were acquired setting the Magic Angle Spinning (MAS) frequency to 16.65 kHz. The effective sample temperature was adjusted to 0 °C. 2D ^{13}C,^{13}C correlation experiments were acquired using DARR (Takegoshi et al., 2003) for mixing, employing a mixing time of 30 ms. To assign the fibril NMR chemical shifts, conventional 3D NCACX and 3D NCOCX were recorded (McDermott et al., 2000; Pauli et al., 2001). For ^{13}C,^{15}N transfers, specific CP-based experiments were employed (Baldus et al., 1998). In addition, 3D CONCA and 3D CANCO experiments were performed to confirm and assign ambiguous residues (Li et al., 2007; Shi et al., 2009). In these experiments, optimal control CP (OC-CP) was used to improve sensitivity (Tošner et al., 2018; Tošner et al., 2021). Long-range interactions were obtained from long mixing time DARR experiments (100, 300, 400, and 600 ms), as well as PAR (De Paëpe et al., 2008) experiments (5, 15, and 20 ms). Dynamic regions of the fibrils were investigated using INEPT instead of CP in the ^{1}H–^{13}C correlation experiments. CCPN (Stevens et al., 2011) was employed to assign, compare and characterize all solid-state NMR spectra.

MD simulations

We used all-atom molecular dynamics (MD) simulations to characterize the conformational dynamics of the experimentally resolved *ex-vivo* fibrils with morphology I and II (PDB 6dso and PDB 6zch). In addition, two models were created based on 6zch with an alternative interface between the two fibril stacks. The fibrils consisted of 2 stacks (6dso and 6zch-derived model1 and 2) or 3 stacks (6zch). Each fibril was modeled as a six-layered stack with 6 × 69 protein residues per stack. In the 6zch-derived model 1, the interface between the two stacks is formed by K29K-E25. In the 6zch-derived model 2, the interface between the two stacks is formed by E25-K24-D22-G1-E55-K56-D59-R61. For fibrils with two stacks, a box length of 156.89 Å was used; for fibrils with three stacks, a box length of 166.60 Å was used. The systems were filled with TIP4P-EW water and neutralized with 0.15 M NaCl. The force-field parameters for the peptides were taken from Amber99sb-*star*-ildn (Lindorff-Larsen et al., 2010). TIP4P-Ew (Horn et al., 2004) was used for the water molecules. For NaCl, we used the Mamatkulov-Schwierz force field parameters (Mamatkulov and Schwierz, 2018). The MD simulations were performed at fixed particle number N, pressure P, and temperature T using the Gromacs simulation package, version 2018 (van der Spoel et al., 2005; Hess et al., 2008). Periodic boundary conditions were applied, and the particle-mesh Ewald method was used for the periodic treatment of Coulombic interactions. Bonds to hydrogen atoms were constrained using LINCS, and a 2 fs time step was used. To equilibrate the system, we first performed an energy minimization with the steepest descent algorithm. All systems were equilibrated for 1 ns, first in the NVT ensemble (canonical ensemble in which the number of particles N, the volume V and the temperature T is fixed), and then in the NPT ensemble (isothermal-isobaric ensemble in which the number of particles N, the pressure p and the temperature T is fixed). For the production run, we performed a 100 ns simulation for each model, employing the velocity rescaling thermostat with stochastic term, with a time constant of $\tau_T = 0.1\ s^{-1}$, and isotropic Parrinello − Rahman pressure coupling, with a time constant of $\tau_p = 5\ s^{-1}$. Coordinates were written every 40 ps. The root mean square fluctuations (RMSF) were calculated from the production run using the last 50 ns of the simulation with the average structure as a reference and after removing translational and rotational motion. The root mean square deviations (RMSD) were calculated from the production run using the last 50 ns of the simulation and using the experimental structure (6dso) as a reference.

CRediT authorship contribution statement

Arpita Sundaria: Conceptualization, Methodology, Investigation, Data curation, Writing – original draft, Writing – review & editing. **Falk Liberta:** Methodology, Investigation. **Dilan Savran:** Methodology, Investigation. **Riddhiman Sarkar:** Methodology, Investigation. **Natascha Rodina:** Methodology, Investigation. **Carsten Peters:** Methodology, Investigation. **Nadine Schwierz:** Methodology, Investigation, Writing – original draft, Writing – review & editing, Supervision. **Christian Haupt:** Writing – review & editing, Supervision. **Matthias Schmidt:** Writing – review & editing, Project administration, Funding acquisition. **Bernd Reif:** Conceptualization, Writing – original draft, Writing – review & editing, Supervision, Project administration, Funding acquisition.

Declaration of Competing Interest

The authors declare that they have no known competing financial interests or personal relationships that could have appeared to influence the work reported in this paper.

Acknowledgements

This work was performed in the framework of the project DFG Re/1435-16 (B.R.) and SCHM 3276/1 (M.S.) of the German Research Foundation (DFG). We are grateful to the Center for Integrated Protein Science Munich (CIPS-M) for financial support. We acknowledge support from the Helmholtz-Gemeinschaft.

Appendix A. Supplementary data

Supplementary data to this article can be found online at https://doi.org/10.1016/j.yjsbx.2022.100069.

References

Andronesi, O.C., Becker, S., Seidel, K., Heise, H., Young, H.S., Baldus, M., 2005. Determination of membrane protein structure and dynamics by magic-angle-spinning solid-state NMR spectroscopy. J. Am. Chem. Soc. 127, 12965–12974.

Baldus, MARC, Petkova, A.T., Herzfeld, JUDITH, Griffin, R.G., 1998. Cross Polarization in the Tilted Frame: Assignment and Spectral Simplification in Heteronuclear Spin Systems. Mol. Phys. 95 (6), 1197–1207.

Bansal, A., Schmidt, M., Rennegarbe, M., Haupt, C., Liberta, F., Stecher, S., Puscalau-Girtu, I., Biedermann, A., Fandrich, M., 2021. AA amyloid fibrils from diseased tissue are structurally different from in vitro formed SAA fibrils. Nat. Commun. 12.

Brunger, A.F., Nienhuis, H.L.A., Bijzet, J., Hazenberg, B.P.C., 2020. Causes of AA amyloidosis: a systematic review. Amyloid 27 (1), 1–12.

Chambers, R.E., Macfarlane, D.G., Whicher, J.T., Dieppe, P.A., 1983. Serum amyloid A-Protein concentration in rheumatoid arthritis and its role in monitoring disease-activity. Ann. Rheum. Dis. 42, 665–667.

Coetzee, G.A., Strachan, A.F., Vanderwesthuyzen, D.R., Hoppe, H.C., Jeenah, M.S., Debeer, F.C., 1986. Serum Amyloid A- containing human High Density Lipoprotein 3 - density, size and apoliporotein composition. J. Biol. Chem. 261, 9644–9651.

De Buck, M., Gouwy, M., Wang, J.M., Van Snick, J., Opdenakker, G., Struyf, S., Van Damme, J., 2016. Structure and Expression of Different Serum Amyloid A (SAA) Variants and their Concentration-Dependent Functions During Host Insults. Curr. Med. Chem. 23, 1725–1755.

De Paëpe, G., Lewandowski, J.R., Loquet, A., Böckmann, A., Griffin, R.G., 2008. Proton assisted recoupling and protein structure determination. J. Chem. Phys. 129 (24), 245101.

Donovan, K.J., Jain, S.K., Silvers, R., Linse, S., Griffin, R.G., 2017. Proton-Assisted Recoupling (PAR) in Peptides and Proteins. J. Phys. Chem. B 121, 10804–10817.

Frame, N.M., Jayaraman, S., Gantz, D.L., Gursky, O., 2017. Serum amyloid A self-assembles with phospholipids to form stable protein-rich nanoparticles with a distinct structure: A hypothetical function of SAA as a “molecular mop” in immune response. J. Struct. Biol. 200 (3), 293–302.

Gursky, O., 2020. Structural Basis for Vital Function and Malfunction of Serum Amyloid A: an Acute-Phase Protein that Wears Hydrophobicity on Its Sleeve. Curr. Atheroscler. Rep. 22.

Heerde, T., Rennegarbe, M., Biedermann, A., Savran, D., Pfeiffer, P., Hitzenberger, M., Baur, J., Puscalau-Girtu, I., Zacharias, M., Schwierz, N., Haupt, C., Schmidt, M., Fändrich, M., 2022. Cryo-EM demonstrates the in vitro proliferation of an ex vivo amyloid fibril morphology by seeding. Nat. Commun. 13, e85.

Hess, B., Kutzner, C., van der Spoel, D., Lindahl, E., 2008. GROMACS 4: Algorithms for highly efficient, load-balanced, and scalable molecular simulation. J. Chem. Theory Comput. 4, 435–447.

Horn, H.W., Swope, W.C., Pitera, J.W., Madura, J.D., Dick, T.J., Hura, G.L., Head-Gordon, T., 2004. Development of an improved four-site water model for biomolecular simulations: TIP4P- Ew. J. Chem. Phys. 120 (20), 9665–9678.

Kofman, T., Grimbert, P., Canoui-Poitrine, F., Zuber, J., Garrigue, V., Mousson, C., Frimat, L., Kamar, N., Couvrat, G., Bouvier, N., Albano, L., Le Thuaut, A., Pillebout, E., Choukroun, G., Couzi, L., Peltier, J., Mariat, C., Delahousse, M., Buchler, M., Le Pogamp, P., Bridoux, F., Pouteil-Noble, C., Lang, P., Audard, V., 2011. Renal Transplantation in Patients With AA Amyloidosis Nephropathy: Results From a French Multicenter Study. Am. J. Transplant. 11, 2423–2431.

Lachmann, H.J., Goodman, H.J.B., Gilbertson, J.A., Gallimore, J.R., Sabin, C.A., Gillmore, J.D., Hawkins, P.N., 2007. Natural history and outcome in systemic AA amyloidosis. N. Engl. J. Med. 356, 2361–2371.

Li, Y., Berthold, D.A., Frericks, H.L., Gennis, R.B., Rienstra, C.M., 2007. Partial C-13 and N-15 chemical-shift assignments of the disulfide-bond-forming enzyme DsbB by 3D magic-angle spinning NMR spectroscopy. Chembiochem 8, 434–442.

Liberta, F., Loerch, S., Rennegarbege, M., Schierhorn, A., Westermark, P., Westermark, G. T., Hazenberg, B.P.C., Grigorieff, N., Fandrich, M., Schmidt, M., 2019a. Cryo-EM fibril structures from systemic AA amyloidosis reveal the species complementarity of pathological amyloids. Nat. Commun. 10, e1104.

Liberta, F., Rennegarbe, M., Rösler, R., Bijzet, J., Wiese, S., Hazenberg, B.P.C., Fändrich, M., 2019b. Morphological and primary structural consistency of fibrils from different AA patients (common variant). Amyloid 26 (3), 164–170.

Lindorff-Larsen, K., Piana, S., Palmo, K., Maragakis, P., Klepeis, J.L., Dror, R.O., Shaw, D. E., 2010. Improved Side-Chain Torsion Potentials for the Amber Ff99sb Protein Force Field. Proteins 78 (8), 1950–1958.

Lu, J.H., Yu, Y.D., Zhu, I., Cheng, Y.F., Sun, P.D., 2014. Structural mechanism of serum amyloid A-mediated inflammatory amyloidosis. Proc. Natl Acad. Sci. U.S.A. 111, 5189–5194.

Mamatkulov, S., Schwierz, N., 2018. Force fields for monovalent and divalent metal cations in TIP3P water based on thermodynamic and kinetic properties. J. Chem. Phys. 148 (7), 074504.

Maszota, M., Karska, N., Spodzieja, M., Ciarkowski, J., Kolodziejczyk, A.S., Rodziewicz-Motowidlo, S., Czaplewska, P., 2015. Structural studies of the C-terminal 19-peptide of serum amyloid A and its Pro -> Ala variants interacting with human cystatin C. J. Mol. Recognit. 28, 413–426.

McDermott, A., Polenova, T., Böckmann, A., Zilm, K.W., Paulsen, E.K., Martin, R.W., Montelione, G.T., 2000. Partial Assignments for uniformly (^{13}C,^{15}N)-enriched BPTI in the solid state. J. Biomol. NMR 16, 209–219.

Pauli, J., Baldus, M., Van Rossum, B.-J., De Groot, H., Oschkinat, H., 2001. Backbone and Side-Chain ^{13}C and ^{15}N Signal Assignments of the a-Spectrin SH3 Domain by Magic Angle Spinning Solid-State NMR at 17.6 Tesla. ChemBioChem 2, 272–281.

Pradhan, T., Annamalai, K., Sarkar, R., Hegenbart, U., Schönland, S., Fändrich, M., Reif, B., 2021. Solid state NMR assignments of a human λ-III immunoglobulin light chain amyloid fibril. Biomol. NMR Assign 15 (1), 9–16.

Prelli, F., Pras, M., Frangione, B., 1987. Degradation and deposition of amyloid AA fibrils are tissue specific. Biochemistry 26, 8251–8256.

Qiang, W., Yau, W.M., Tycko, R., 2011. Structural Evolution of Iowa Mutant beta-Amyloid Fibrils from Polymorphic to Homogeneous States under Repeated Seeded Growth. J. Am. Chem. Soc. 133, 4018–4029.

Rennegarbe, M., Lenter, I., Schierhorn, A., Sawilla, R., Haupt, C., 2017. Influence of C-terminal truncation of murine Serum amyloid A on fibril structure. Sci. Rep. 7.

Sack, G.H., 2018. Serum amyloid A - a review. Mol. Med. 24.

Sayed, R.H., Hawkins, P.N., Lachmann, H.J., 2015. Emerging treatments for amyloidosis. Kidney Int. 87 (3), 516–526.

Schönfelder, J., Pfeiffer, P.B., Pradhan, T., Bijzet, J., Hazenberg, B.P.C., Schönland, S.O., Hegenbart, U., Reif, B., Haupt, C., Fändrich, M., 2021. Protease resistance of ex vivo amyloid fibrils implies the proteolytic selection of disease-associated fibril morphologies. Amyloid 28 (4), 243–251.

Shi, L., Lake, E.M.R., Ahmed, M.A.M., Brown, L.S., Ladizhansky, V., 2009. Solid-state NMR study of proteorhodopsin in the lipid environment: Secondary structure and dynamics. Biochim. Biophys. Acta 1788 (12), 2563–2574.

Shridas, P., Tannock, L.R., 2019. Role of serum amyloid A in atherosclerosis. Curr. Opin. Lipidol. 30, 320–325.

Solomon, A., Richey, T., Murphy, C.L., Weiss, D.T., Wall, J.S., Westermark, G.T., Westermark, P., 2007. Amyloidogenic potential of foie gras. Proc. Natl. Acad. Sci. U. S.A. 104, 10998–11001.

Stevens, T.J., Fogh, R.H., Boucher, W., Higman, V.A., Eisenmenger, F., Bardiaux, B., van Rossum, B.-J., Oschkinat, H., Laue, E.D., 2011. A software framework for analysing solid-state MAS NMR data. J. Biomol. NMR 51 (4), 437–447.

Stix, B., Kahne, T., Sletten, K., Raynes, J., Roessner, A., Rocken, C., 2001. Proteolysis of AA amyloid fibril proteins by matrix metalloproteinases-1,-2, and-3. Am. J. Pathol. 159, 561–570.

Takegoshi, K., Nakamura, S., Terao, T., 2003. C-13-H-1 dipolar-driven C-13-C-13 recoupling without C-13 rf irradiation in nuclear magnetic resonance of rotating solids. J. Chem. Phys. 118, 2325–2341.

Tanaka, M., Kawakami, T., Okino, N., Sasaki, K., Nakanishi, K., Takase, H., Yamada, T., Mukai, T., 2018. Acceleration of amyloid fibril formation by carboxyl-terminal truncation of human serum amyloid A. Arch. Biochem. Biophys. 639, 9–15.

Tošner, Z., Sarkar, R., Becker-Baldus, J., Glaubitz, C., Wegner, S., Engelke, F., Glaser, S. J., Reif, B., 2018. Overcoming volume selectivity of dipolar recoupling in biological solid-state NMR. Angew. Chem. Int. Ed. Engl. 57, 14514–14518.

Tošner, Z., Brandl, M.J., Blahut, J., Glaser, S.J., Reif, B., 2021. Maximizing efficiency of dipolar recoupling in solid-state NMR using optimal control sequences. Sci. Adv. 7, eabj5913.

Uhlar, C.M., Whitehead, A.S., 1999. Serum amyloid A, the major vertebrate acute-phase reactant. Eur. J. Biochem. 265, 501–523.

van der Hilst, J.C.H., Yamada, T., den Camp, H., van der Meer, J.W.M., Drenth, J.P.H., Simon, A., 2008. Increased susceptibility of serum amyloid A 1.1 to degradation by MMP-1: potential explanation for higher risk of type AA amyloidosis. Rheumatology 47, 1651–1654.

van der Spoel, D., Lindahl, E., Hess, B., Groenhof, G., Mark, A.E., Berendsen, H.J.C., 2005. GROMACS: Fast, flexible, and free. J. Comput. Chem. 26, 1701–1718.

Westermark, G.T., Sletten, K., Westermark, P., 1989. Massive vascular AA-Amyloidosis - A histologically and biochemically distinctive subtype of reactive systemic amyloidosis Scan. J. Immunol. 30, 605–613.

Westermark, G.T., Westermark, P., 2005. Purification of amyloid protein AA subspecies from amyloid-rich human tissues. Methods Mol. Biol. 299, 243–254.

Westermark, G.T., Westermark, P., 2009. Serum amyloid A and protein AA: Molecular mechanisms of a transmissible amyloidosis. FEBS Lett. 583, 2685–2690.

Zahedi, K., Gonnerman, W.A., Debeer, F.C., Debeer, M.C., Steel, D.M., Sipe, J.D., Whitehead, A.S., 1991. Major acute-phase reactant synthesis during chronic inflammation in amyloid-susceptible and amyloid-resistant mouse strains. Inflammation 15, 1–14.